View metadata, citation and similar papers at core.ac.uk
brought to you by CORE
provided by DSpace@MIT

Thermospheric Poleward Wind Surge at Mid-Latitudes During Great Storm Intervals

Shun-Rong Zhang[1,*], Philip J. Erickson[1], John C. Foster[1], John M. Holt[1], Anthea J. Coster[1], Jonathan J. Makela[2], John Noto[3], John W. Meriwether[4], Brian J. Harding[2], Juanita Riccobono[3] and Robert B. Kerr[3]

1 MIT Haystack Observatory, Westford, MA, USA

2 Department of Electrical and Computer Engineering, *University of Illinois at Urbana-Champaign, Urbana, Illinois, USA*

3 *Scientific Solution, Inc., Chelmsford, MA, USA*

4 Department of Physics and Astronomy, Clemson University, Clemson, SC, USA

*** Correspondence:**

Dr. Shunrong Zhang (shunrong@haystack.mit.edu)

MIT Haystack Observatory

Off Route 40

Westford, MA 01886

USA

Key points

1. Pre-midnight poleward wind surge at 100m/s, preceded by 300m/s westward winds
2. No equatorward wind surge developed throughout the night
2. Disturbance wind driven by Subauroral Polarization Streams and Coriolis force

Abstract

We report a significant poleward surge in thermospheric winds at subauroral and mid latitudes following the 17-18 March 2015 great geomagnetic storm. This pre-midnight surge is preceded by strong westward winds. These disturbances were observed over three sites with geodetic latitudes 35-42^{o}N in the American sector by Fabry-Perot interferometers at 630-nm wavelength. Prior to the wind disturbances, subauroral polarization streams (SAPS), were measured by the Millstone Hill incoherent scatter radar between 20-02 UT. We identify the observed neutral wind variations as driven by SAPS, through a scenario where strong ion flows cause a westward neutral wind, subsequently establishing a poleward wind surge due to the poleward Coriolis force on that westward wind. These regional disturbances appear to have prevented the well-known storm time equatorward wind surge from propagating into low latitudes, with the consequence that the classic disturbance dynamo mechanism failed to occur.

1. Introduction

An equatorward surge of thermospheric meridional neutral wind at mid-latitudes is a common dynamic feature of Earth's neutral atmosphere during geomagnetic storms. Numerous studies have shown in detail how storm time momentum and energetic inputs perturb the high-latitude ionosphere and thermosphere, with subsequent equatorward propagation of disturbances [see reviews, Matuura, 1972; Prolss, 1995; Buonsanto, 1999; Mendillo, 2006]. In particular, the storm time equatorward wind generated by impulsive polar latitude heating processes can be very strong at night (1) when disturbance effects add to the quiet time equatorward neutral circulation [Rishbeth, 1989], and (2) when high-latitude convection is enhanced and expanded equatorward causing a significant anti-sunward ion flow [e.g., Straus and Schulz, 1976]. Due to the Coriolis force, the equatorward wind surge can subsequently drive a westward neutral wind disturbance as it reaches mid- and low-latitudes. These wind disturbances are at the heart of the important ionospheric dynamo effect [Blanc and Richmond, 1980; Fuller-Rowell et al., 2002] and equatorward wind surges have been the subject of prior studies [e.g., Meriwether, 2008].

However, equatorward wind surges do not necessarily occur during every storm. In fact, the disturbance wind undergoes substantial variability with local time, season and solar activity for a given location. Fejer et al. [2002] showed that at Millstone Hill (MH, 42.6^{o}N, 71.5^{o}W; geodetic), storm time winds sometimes turn poleward following a midnight or post-midnight equatorward surge (in particular for solar minimum). The pre-midnight meridional wind disturbance, however, is generally weak and equatorward, occasionally with a very small and brief poleward turning. The poleward wind surge can be also seen as traveling atmosphere disturbances (TADs) from the opposite hemisphere [e.g., Shiokawa et al., 2003].

71 This paper reports a fundamentally different neutral wind scenario observed over three
72 sites at mid and subauroral latitudes during the 17-18 March 2015 great storm. During
73 this event, the pre-midnight meridional wind turns poleward and remains in this direction
74 for a few hours. Using a joint analysis of incoherent scatter radar (ISR) and Fabry-Perot
75 interferometer (FPI) observations along with first-principles model simulations, we show
76 in this paper that the anomalous poleward wind originated from the Subauroral
77 Polarization Stream (SAPS) [Foster and Vo, 2002], a characteristic storm time
78 magnetosphere-ionosphere coupling feature within a relatively narrow region of low
79 ionospheric conductivity between the auroral precipitation zone and the plasmasphere
80 boundary layer [Carpenter and Lemaire, 2004]. Strong SAPS flows overlap the
81 plasmasphere edge and provide a significant convective force moving plasma against
82 corotation from the dusk sector toward the noontime cusp in storm enhanced density
83 (SED) features [Foster, 1993; Kelly et al., 2004], also known as the dusk effect
84 [Mendillo, 2006]. Sunward ion flow in the late afternoon sector (with a poleward
85 component) also causes SED plasma to drift upwards at subauroral latitudes into regions
86 where recombination rates are significantly reduced, leading to high electron density
87 values [Heelis, 2008]. Strong plasma flow has reportedly produced enhanced neutral
88 westward winds [e.g., Wang H. et al., 2011] due to strong ion drag effects. TIEGCM
89 simulations [Wang W. et al., 2012] confirm expected ion drag effects in the
90 thermospheric temperature and zonal winds on a global scale.
91
92 **2. Observations and Analysis Procedure**
93
94 Following the arrival of a Coronal Mass Ejection (CME) and under the influence of high-
95 speed solar wind streams, severe/great geomagnetic disturbances occurred for an
96 extended period starting on 17 March 2015 (Figures 1a-b). Interplanetary Magnetic Field
97 (IMF) northward component Bz hourly values in Geocentric Solar Magnetospheric
98 (GSM) coordinates fell to -14 nT between 05 - 08 UT, and then underwent a 12-hour
99 long sustained negative disturbance of ~ -17 nT between 12 - 24 UT on the 17th. During
100 this time, the hourly Dst index dropped to a minimum of -227 nT at 23 UT. The 3-hourly

Kp value jumped to 5- with the initial Bz negative excursion, reaching between 8- and 7+ during the large and long-lasting drop in Bz.

These geospace disturbances caused a series of significant changes in earth's ionosphere and thermosphere. Figure 1(c) plots TEC disturbances, as derived from global GPS ground receiver data by MIT Haystack Observatory MAPGPS software [Rideout and Coster, 2006]. The TEC disturbances are defined here as the mean TEC value in each 3^o latitude bin over 30-50^o N geodetic latitudes over the MH longitude (70-80^o W) after undisturbed background TEC has been subtracted using a monthly-average based empirical model [Chen et al., 2014]. An initial positive disturbance of more than 50% is seen poleward of MH following the first Bz equatorward turning. A narrow enhancement zone at 18 UT is visible, and subsequent enhancements extended and expanded from MH latitudes at 21 UT to lower latitudes at 23 UT. Subsequent sharp decreases of ~ 50% expanded from 50^o N at 20 UT to 37^o N within 4 hours.

This equatorward moving density reduction zone eventually remained at 38-42^oN between 24-05 UT. It is during these pre-midnight hours, and within the midlatitude trough, that both SAPS and neutral wind disturbances were observed (Section 3). The presence of a SAPS flow channel is further evidenced by MH ISR observations (Section 3). The ~50% TEC enhancement seen equatorward of the trough is a typical SED characteristic, and is a result of plasmaspheric erosion associated with SAPS. Later sections will present these radar observations and will discuss the connection between SAPS and neutral wind disturbances.

During this storm, an international observation campaign along the meridian circle of 60^oW/120^oE longitude was conducted. In particular, excellent ionospheric plasma information from ISRs and neutral atmosphere information from FPIs is available in the western hemisphere, along with other observational facilities supported by the Chinese Meridian Project [Wang, 2010] and other institutions in the eastern hemisphere.

131 At mid-latitudes, the MH ISR operated in an experimental sequence using both zenith
132 and steerable antennas providing local, regional, and wide coverage. The wide coverage
133 is provided by low (6^o) elevation radar scans from north to west of Millstone Hill while
134 regional coverage uses 45^o elevation positions in north and west directions combined
135 with zenith observations. Combining line-of-sight (LOS) ion velocities in these multiple
136 directions allows derivation of key components of F-region ion velocity perpendicular to
137 the magnetic field: VperE, eastward perpendicular to magnetic field **B**, and VperN,
138 poleward perpendicular to **B**. VperE is determined to the northwest of MH at ~(47^oN,
139 89^oW) from the west-looking data using azimuths in the (-100, -45) degree range. VperN
140 is determined for MH north at ~(53^oN, 75^oW) from low elevation north-looking data such
141 that LOS is nearly perpendicular to the magnetic field. These observations provide
142 evidence of SAPS.
143
144 FPIs observing the thermospheric 630.0-nm emission arising from dissociative
145 recombination of O_2^+ provide LOS measurements of neutral winds at typical emission
146 heights of ~250 km altitude. Data from three sites in North America were used in this
147 study. At MH, the emission is detected from look directions in the north, east, south,
148 west (all with 45^o elevation) and zenith. The other two FPI redline sites are from the
149 North American Thermosphere-Ionosphere Observing Network (NATION) [Makela et
150 al., 2014]: Urbana Atmospheric Observatory (UAO, 40.13^oN, 88.20^oW) and Pisgah
151 Astronomical Research Institute (PAR, 35.2^oN, 82.85^oW) [Makela et al., 2011]. They
152 have similar look angles to MH, with the addition of a pointing direction upward along **B.**
153 A typical observational cycle takes 12 min for NATION sites (15 min for MH), and data
154 are analyzed using the methodology described in Harding et al. [2014]. During the 17-18
155 March night, the skies over PAR became partly cloudy after 0630 UT on 18 March, and
156 the skies over UAO became partly cloudy after ~03 UT, but these facts do not
157 significantly affect results for the key period addressed by this work. Additionally, the
158 apparent vertical wind conditions described in Makela et al. [2014] did not seem to occur
159 during the observations reported here, making the small vertical wind assumption,
160 typically used when analyzing FPI observations, valid. To estimate the neutral wind

vector based on LOS FPI observations, we follow a procedure where the vector velocity is determined through a least-squared fit algorithm using the combined LOS data from all directions within 36 min (45 min for MH), weighted by the LOS errors. Standard deviations on the resulting vector neutral winds are also given.

3. Superstorm Thermospheric and Ionospheric Response

FPI observations during the evening of 17-18 March began just after the main phase of the storm at the time of maximum ring current intensity / minimum Dst value, as Bz started to return to positive values. At MH (Figure 2), a strong westward zonal wind of 300 m/s was already established, at a 350 m/s offset from its monthly mean in the eastward direction. The strong westward wind then weakened after 02 UT, and stayed at 200 m/s for 2 hours. During the next 3 hours, the westward zonal wind eventually returned to its monthly mean and the disturbance vanished after local midnight. The meridional wind component started slightly equatorward then subsequently became significantly poleward, eventually reaching 100 m/s at 0230-0300 UT (~22 LT). The poleward wind surge was significant between 2030 and 2230 LT, primarily before midnight. Following this period, the meridional wind returned to its monthly mean value and remained in line with monthly averages without any further equatorward or poleward surges.

FPI observations at UAO at latitudes comparable to MH show very similar features. In particular, a strong westward zonal wind lasting ~2 hours was followed by a 2-hour long poleward meridional wind surge, reaching 100 m/s at 0230 UT. The PAR FPI station is 5^{o} to the south of UAO and MH, and the poleward wind abatement, reaching 100 m/s at 0300 UT, is preceded by a strong westward enhancement for ~2 hours. The westward wind enhancement is not as strong at PAR as at the other two higher latitude sites.

Prior to the occurrence of these neutral wind disturbances, strong ionospheric disturbances were observed such as the midlatitude trough, SEDs, and associated SAPS

flows. Figure 3 shows VperE (perpendicular eastward, a) in the west and VperN (perpendicular northward, b) in the north of MH on 17-18 March as well as later on 19 March, where observations for the latter half of the 18th and first half of the 19th can be considered representative of normal ionospheric conditions due to relatively low magnetic activity.

The magnetically zonal ion drift, VperE, turned westward at 20 UT. In the next 5 hours, this westward drift remained very strong at 500-750 m/s. We identified the high-speed ion flow as SAPS since it is situated near the low density (midlatitude trough) region as evidenced in TEC (Figure 1c) and also in the ISR measured electron content IEC (Figure 3d). SAPS features are also associated with SED passage over MH, prior to the SAPS local onset, as shown in the TEC plume equatorward of the trough (Figure 1c) and in the IEC peak at 20UT (Figure 3c). Since the ion speed is faster than the speed of the neutrals, SAPS will accordingly drive the neutrals in the same direction. MH and UAO zonal winds in Figure 2 are shown in Figure 3(e) to highlight this neutral and ion velocity connection. Even though the exact onset time of the westward neutral wind enhancements are unknown due to lack of data prior to 00 UT, the enhancements weakened around 02-03UT when the large westward ion drift disappeared. The largest westward wind surge (~400 m/s) is at UAO where the TEC drop appears the most significant, and therefore SAPS peak velocities are expected to be the strongest.

The neutral wind disturbance, and in particular the poleward surge, can be seen in the upward ion drift Vz at 250 km (Figure 3c). Between 01-05 UT on 18 March when electric fields are quiet, Vz is more negative (downward) compared to the reference, suggesting that the poleward wind surge makes a significant contribution.

The radar data shows also a strong poleward ion drift VperN at ~55^{o}N, in particular, between 20-23 UT. Combining these northward and westward components, it is likely that the sunward drift is a significant factor in producing the large observed SED plumes in TEC and IEC data.

4. Simulation of Wind Effects

4.1 March 17th Event Summary

The observations described in Section 3 are consistent with the following timeline of ionosphere and thermosphere processes during the 17-18 March superstorm: (1) At ~21 UT on 17 March, SED plumes are present, observed as TEC and IEC enhancements, along with onset of strong SAPS westward ion drift of >500 m/s peaking in the midlatitude trough of the American sector; (2) Starting at about 22 UT, a strong westward neutral wind appears (with greater amplitude in the trough region of ~40 - 42^{o}N latitude as compared to 35^{o}N) and lasts for 4 hours until 02 UT on 18 March. After 02 UT, the zonal wind amplitude decreased dramatically (at higher latitudes) or gradually (at lower latitudes); and (3) At 03 UT, a poleward wind surge of ~100 m/s occurs. We posit that the chain of events from (1) to (3) are a result of ion-neutral coupling and thermospheric dynamical processes. In particular, the westward neutral wind characteristics described in (2) are attributable to the well-known ion drag effect following the onset of SAPS described in (1). Our proposition is further indicated by the observation that westward neutral wind anomalies disappeared when SAPS forcing disappeared, with the effects strongest in the area of the deepest midlatitude trough. Subsequently, the poleward wind surge described in (3) is produced following strong westward winds as described in (2) because of the poleward Coriolis force arising from significant westward wind amplitudes.

4.2 Simulated F-region westward ion drift effects

To explore the validity of this scenario, an ion-neutral coupling simulation was conducted with parameters characteristic of mid-latitudes near Millstone Hill. This relatively simple simulation was designed to study the basic proposed mechanism and its general features, rather than reproducing all observational details. The numerical experiment utilizes a local ionosphere-thermosphere wind coupling model. The ionospheric model [Zhang and Huang, 1995; Zhang et al., 2003] solves the equation of mass continuity for multiple ions

and the equation of momentum for O^+. Ionospheric temperatures are set to the empirical ISR Ionospheric Model (ISRIM) for MH [Zhang et al., 2005; 2007b]. The non-disturbance electric field is specified by the local electric fields derived from the statistical Millstone Hill – Sondrestrom convection model [Zhang et al., 2007a]. Neutral densities and temperatures are specified by the NRL-MSIS model [Picone et al., 2002]. The neutral wind calculation is based on solving the momentum equation for the neutral gas where pressure gradients are derived from the NRL-MSIS model. A resolution of 2-min in time and 2-km in altitude is used. Other details of the simulation are described

A baseline / reference run for medium solar activity levels at equinox, corresponding to 17 March 2015 conditions, was performed without imposing the observed westward ion drift. A second run included a 500 m/s westward ion drift imposed during 18-21 LT (23-02 UT). This 500 m/s value represents a modest enhancement in zonal ion velocity compared to the ISR measured SAPS speed on 17 March (cf. Section 3). The top panel of Figure 4 plots the calculated model profiles of electron density and neutral winds at 1930 LT, 1.5 hours into the strong westward ion drift injection event. The middle panel shows differential changes in calculated poleward and eastward winds relative to the reference run. The differential results clearly show a build-up of westward winds within one hour following SAPS turn-on, saturating at 300 m/s at ~1930 LT. This ~200 m/s difference in flow speeds between ions and neutrals created frictional heating leading to neutral temperature increases (not shown). The poleward wind showed a different behavior, gradually increasing in speed but at slower rates compared to westward wind increases. In particular, northern wind differential values peaked at 130 m/s at ~2130 LT, with a delay of ~2 hours following westward neutral flow saturation and ~3.5 hours following SAPS initiation. These time constants are governed by background thermospheric density and temperature, which undergo substantial storm time changes (and therefore the real response times can be quite different from simulated results.) In the simulation, the Coriolis force is the only mechanism that connects the zonal and meridional winds, so the key finding is that poleward wind buildup is caused by Coriolis force effects in the north

direction because of westward neutral motion, with the characteristic time delay in storm time variations between the two components as another sign of Coriolis forcing.

The third panel of Figure 4 plots ionospheric electron density differential response to strong westward ion drift. The peak height, hmF2, dropped by ~55 km during the period of significant poleward wind, and NmF2 dropped by ~80% after the westward ion drift ceased. In this numerical experiment, the electron density reduction is achieved by the induced poleward winds only, but an increase in the ion recombination rate caused by frictional heating can further reduce the F-region electron density [Schunk et al., 1975].

5. Discussion

Reproducing all observational details with the numerical experiment in Section 4 is not possible because of the simulation's simplified treatment of ion and neutral temperatures and neutral densities, which in reality are likely subject to large offsets from the empirical model specifications used in this storm study. In particular, we have ignored the potential presence of meridional pressure gradients to the north of MH, produced by the same auroral heating processes that likely would generate an equatorward wind surge. The simulated poleward surge produced by Coriolis force action is smooth and gradual in time. This is quite similar to FPI observations at the lower latitude site, PAR. By contrast, at the higher latitude of MH the observed poleward surge grows faster than in the simulation. A more precise neutral response simulation would require a better specification of storm time neutral density and temperature. In general, more sophisticated modeling is needed to put the regional observations into correct global context and to better explain observational features. However, the initial simplified simulation presented here is sufficient to demonstrate that ion-neutral coupling and Coriolis force effects are likely to play fundamental roles in observed wind dynamics.

Coriolis force effects on westward neutral wind amplitude were noted in an earlier numerical experiment by Forbes and Roble [1990]. Hagan and Sipler [1991] also report a

similar set of observed ionospheric and thermospheric storm time effects with smaller westward wind and minor meridional wind abatement during the 7-10 March 1989 storm at MH. They pointed out that westward winds caused diminishment of equatorward wind surges due to Coriolis forces. Hernandez et al. [1982] reported a converging wind system measured by the FPI over Fritz Park (39.9°N, 105.5°W) during two major storms where similar ion-neutral interaction was speculated for the south of the site. It appears that large westward winds, the poleward turning of the wind, and low electron densities are all potential consequences of ion-neutral coupling in some large storm events such as presented here.

During large geospace storm intervals, TADs are often observed, and in fact poleward winds observed at lower mid-latitudes in Asia were explained as resulting from TAD passage with a disturbance source region in the south [e.g., Shiokawa et al., 2003]. This study, however, does not show obvious signs of propagating waves as in the TAD scenario. In particular, the poleward wind surge and westward wind enhancement appear stronger at subauroral latitudes than at lower latitudes, counter to expectations of a TAD mechanism to the south generating atmospheric waves. TADs from sources to the north would cause equatorward wind perturbations, not poleward as observed.

6. Summary and conclusion

Strong geospace disturbances during the 17-18 March 2015 superstorm produced intense electric fields at subauroral and mid-latitudes. SED plumes shown in TEC and ISR electron content enhancements over the northeast US are present prior to 21 UT before passage of the midlatitude trough. A strong westward ion drift, identified as SAPS, then developed during 21-02 UT, as observed by the Millstone Hill ISR. This drift, drove neutral particles westward, causing a strong westward neutral wind (~300 m/s) observed by multiple FPIs between 35-42^{o}N latitudes in the American sector. Later in the event, a poleward neutral wind response occurred due to Coriolis force effects on the westward neutral wind. The poleward wind, directly observed by the FPIs, eventually reached 100

m/s amplitude in a few hours following the onset of SAPS. A simplified numerical model with coupling of ionospheric density and thermospheric neutral winds is able to demonstrate response characteristics of this mechanism that reasonably match general observational features. We conclude that unusual neutral wind disturbances in both zonal and meridional directions have their ultimate source in the SAPS electric field which generates substantial ion flows and leads to strong ion-neutral interaction.

We point out that the observed pre-midnight storm time surge in the poleward wind implies a regional circulation background that may prevent propagation of the auroral heating produced equatorward wind surge to lower latitudes, and would therefore prevent development of the classic disturbance dynamo. If correct, this mechanism may substantially influence the storm time low latitude and equatorial electrodynamic response in some cases [Fejer and Scherliess, 1995; Maruyama et al., 2005; Lu et al., 2012]. Thus, further investigation is needed to characterize westward ion drifts at subauroral latitudes, including SAPS, as a significant driving factor, and to understand more fully how the SAPS driven neutral wind disturbances are affected by storm-time ionosphere and thermosphere conditions.

Acknowledgements

Ground-based observational data from FPIs and the Millstone Hill ISR are all obtained through the Madrigal database system (www.openmadrigal.org) developed and maintained by MIT Haystack Observatory. Dst and Kp data are obtained from the World Data Center at Kyoto University (http://wdc.kugi.kyoto-u.ac.jp/wdc/Sec3.html). The solar wind data are obtained from the Advanced Composition Explorer (ACE) satellite, and the real-time 1-hour average IMF Bz data sets are obtained from the archive at the NOAA Space Weather Prediction Center (ftp://ftp.swpc.noaa.gov/pub/lists/ace2/). ISR observations and analysis at MIT Haystack Observatory are supported by cooperative agreement AGS-1242204 between the National Science Foundation and the Massachusetts Institute of Technology. SRZ and PJE also acknowledge NASA LWS

370 funding support (NNX15AB83G). FPI measurements at Millstone Hill are supported by
371 NSF grant AGS-0640745 to the University Corporation for Atmospheric Research, and at
372 UAO and PAR by National Science Foundation CEDAR grants AGS-1138998 and AGS-
373 1138931 to the University of Illinois and Clemson University, respectively. SRZ is
374 indebted to Wenbin Wang, Tim Fuller-Rowell, and members of the NASA LWS topside
375 team for valuable comments on initial results of this research. GPS TEC data products
376 and access through the Madrigal distributed data system are provided to the community
377 by the Massachusetts Institute of Technology under support from US National Science
378 Foundation grant AGS-1242204. Data for the TEC processing is provided from the
379 following organizations: UNAVCO, Scripps Orbit and Permanent Array Center, Institut
380 Geographique National, France, International GNSS Service, The Crustal Dynamics Data
381 Information System (CDDIS), National Geodetic Survey, Instituto Brasileiro de
382 Geografia e Estatística, RAMSAC CORS of Instituto Geográfico Nacional del la
383 República Agentina, Arecibo Observatory, Low-Latitude Ionospheric Sensor Network
384 (LISN), Topcon Positioning Systems, Inc., Canadian High Arctic Ionospheric Network,
385 Institute of Geology and Geophysics (Chinese Academy of Sciences), China
386 Meterorology Administration, Centro di Ricerche Sismogiche, Système d'Observation du
387 Niveau des Eaux Littorales (SONEL), RENAG : REseau NAtional GPS permanent, and
388 GeoNet - the official source of geological hazard information for New Zealand.
389
390
391

References

Blanc, M., and A. D. Richmond (1980), The ionospheric disturbance dynamo, J. Geophys. Res., 85, 1669–1686.

Buonsanto, M. J. (1999), Ionospheric storms—A review, Space Sci. Rev., 88, 563–601.

Buonsanto, M. J., Foster, J. C., Galasso, A. D., Sipler, D. P., Holt, J. M. (1990) Neutral Winds and Thermosphere/Ionosphere Coupling and Energetics During the Geomagnetic Disturbances of March 6–10, 1989. J. Geophys. Res. 95: pp. 21033-21050

Carpenter, D. and J. Lemaire (2004), The plasmasphere boundary layer, Ann. Geophys. 22, 4291–4298.

Chen, Z., S.-R. Zhang, A. J. Coster, and G. Fang (2015), EOF analysis and modeling of GPS TEC climatology over North America, J. Geophys. Res. Space Physics, 120, doi:10.1002/2014JA020837.

Fejer, B. G. (2002), Climatology and storm time dependence of nighttime thermospheric neutral winds over Millstone Hill, J. Geophys. Res., 107(A5), 1052, doi:10.1029/2001JA000300.

Fejer, B. G., and L. Scherliess (1995), Time dependent response of equatorial ionospheric electric fields to magnetospheric disturbances, Geophys. Res. Lett., 22(7), 851–854, doi:10.1029/95GL00390.

Foster, J. C. (1993), Storm time plasma transport at middle and high latitudes, *J. Geophys. Res.*, 98, 1675–1690.

Foster, J. C., and H. B. Vo (2002), Average Characteristics and Activity Dependence of the Subauroral Polarization Stream, *J. Geophys. Res.*, 107(A12),1475, doi: 10.1029/2002JA009409.

Forbes, J. M., and R. G. Roble (1990), Thermosphere-ionosphere coupling: An experiment in interactive modeling, J. Geophys. Res., 95(A1), 201, doi:10.1029/JA095iA01p00201.

Fuller-Rowell, T. J., G. H. Millward, A. D. Richmond, and M. V. Codrescu (2002), Storm-time changes in the upper atmosphere at low latitudes, J. Atmos. Sol. Terr. Phys., 64, 1383.

435 Hagan, M. E., and D. P. Sipler (1991), Combined incoherent scatter radar and Fabry-
436 Perot interferometer measurements of frictional heating effects over Millstone Hill during
437 March 7–10, 1989, J. Geophys. Res., 96(A1), 289, doi:10.1029/90JA02250.
438
439 Harding, B. J., T. W. Gehrels, and J. J. Makela (2014), Nonlinear regression
440 method for estimating neutral wind and temperature from Fabry–Perot
441 interferometer data, Appl. Opt., 53(4), 666.
442 Heelis, R. A. (2008) Low- and Middle-Latitude Ionospheric Dynamics Associated with
443 Magnetic Storms, in Midlatitude Ionospheric Dynamics and Disturbances (eds P. M.
444 Kintner, A. J. Coster, T. Fuller-Rowell, A. J. Mannucci, M. Mendillo and R. Heelis),
445 American Geophysical Union, Washington, D. C.. doi: 10.1029/181GM06
446 Hernandez, G., R. G. Roble, E. C. Ridley, and J. H. Allen (1982), Thermospheric
447 response observed over Fritz Peak, Colorado, during two large geomagnetic storms near
448 Solar Cycle Maximum, *J. Geophys. Res.*, *87*(A11), 9181-9192, doi:10.1029/JA087.
449
450
451 Lu, G., L. Goncharenko, M. J. Nicolls, A. Maute, A. Coster, and L. J. Paxton (2012),
452 Ionospheric and thermospheric variations associated with prompt penetration electric
453 fields, J. Geophys. Res., 117, A08312, doi:10.1029/2012JA017769.
454
455 Makela, J. J., J. W. Meriwether, Y. Huang, and P. J. Sherwood (2011), Simulation and
456 analysis of a multi-order imaging Fabry–Perot interferometer for the study of
457 thermospheric winds and temperatures, Appl. Opt., 50, 4403-4416.
458
459 Makela, J. J., et al. (2014), Storm time response of the midlatitude thermosphere:
460 Observations from a network of Fabry-Perot interferometers, J. Geophys. Res. Space
461 Physics, 119, 6758–6773, doi:10.1002/2014JA019832.
462
463 Matuura, N. (1972), Theoretical models of ionospheric storms, Space Sci. Rev., 13, 124–
464 189.
465
466 Mendillo, M. (2006), Storms in the ionosphere: Patterns and processes for total electron
467 content, Rev. Geophys., 44, RG4001, doi:10.1029/2005RG000193.
468
469 Maruyama, N., A. D. Richmond, T. J. Fuller-Rowell, M. V. Codrescu, S. Sazykin, F. R.
470 Toffoletto, R. W. Spiro, and G. H. Millward (2005), Interaction between direct
471 penetration and disturbance dynamo electric fields in the storm-time equatorial
472 ionosphere, Geophys. Res. Lett., 32, L17105, doi:10.1029/2005GL023763.
473
474 Picone, J. M., A. E. Hedin, D. P. Drob, and A. C. Aikin, NRLMSISE-00 empirical model
475 of the atmosphere: Statistical comparisons and scientific issues, J. Geophys. Res.,
476 107(A12), 1468, doi:10.1029/2002JA009430, 2002.

Prölss, G. W. (1995), Ionospheric F-region storms, in Handbook of Atmospheric Electrodynamics, vol. 2, edited by H. Volland, chap. 8, pp. 195–248, CRC Press, Boca Raton, Fla.

Rideout, W., and A. Coster (2006), Automated GPS processing for global total electron content data, GPS Solut., 10, 219–228, doi:10.1007/s10291-006-0029-5.

Rishbeth, H. (1998), How the thermospheric circulation affects the ionospheric F2-layer, J. Atmo. Sol.-Terr. Phys., 60(14), 1385–1402.

Schunk, R. W., W. J. Raitt, and P. M. Banks (1975), Effect of electric fields on the daytime high-latitude E and F regions, J. Geophys. Res., 80, 3121.

Shiokawa, K., et al. (2003), Thermospheric wind during a storm-time large-scale traveling ionospheric disturbance, J. Geophys. Res., 108, 1423, doi:10.1029/2003JA010001, A12.

Straus, J.M., Schulz, M. (1976), Magnetospheric Convection and Upper Atmospheric Dynamics'. J. Geophys. Res. 81, 5822-5832.

Wang, C. (2010), New Chains of Space Weather Monitoring Stations in China. Space Weather, 8: n/a. doi: 10.1029/2010SW000603

Wang, W., E. R. Talaat, A. G. Burns, B. Emery, S. Hsieh, J. Lei, and J. Xu (2012), Thermosphere and ionosphere response to subauroral polarization streams (SAPS): Model simulations, J. Geophys. Res., 117, A07301, doi:10.1029/2012JA017656.

Wang, H., H. Lühr, K. Häusler, and P. Ritter (2011), Effect of subauroral polarization streams on the thermosphere: A statistical study, J. Geophys. Res., 116, A03312, doi:10.1029/2010JA016236.

Zhang S.-R. and X.-Y. Huang (1995), A Numerical Study of Ionospheric Profiles for Mid-Latitudes, Ann Geophysicae, 13, 551-557.

Zhang, S.-R. W. L. Oliver, J. M. Holt, and S. Fukao (2003), Ionospheric data assimilation: Comparison of extracted parameters using full density profiles and key parameters, J. Geophys. Res. 108, 10.1029/2002JA009521.

Zhang, S.-R., J. M. Holt, A. P. van Eyken, M. McCready, C. Amory-Mazaudier, S. Fukao, and M. Sulzer (2005), Ionospheric local model and climatology from long-term databases of multiple incoherent scatter radars, Geophys. Res. Lett., 32, L20102, doi:10.1029/2005GL023603

521 Zhang, S.-R. and J. M. Holt (2007a), Ionospheric Climatology and Variability from
522 Long-term and Multiple Incoherent Scatter Radar Observations: Climatology in Eastern
523 American Sector, J. Geophys. Res., 12, A06328, doi:10.1029/2006JA012206
524
525 Zhang, S.-R., J. M. Holt, and M. McReady (2007b), High latitude convection model
526 based on long-term incoherent scatter radar observations in North America, J. Atmos.
527 Sol.-Terr. Phys., 69, 1273-1291, doi:10.1016/j.jastp.2006.08.017
528

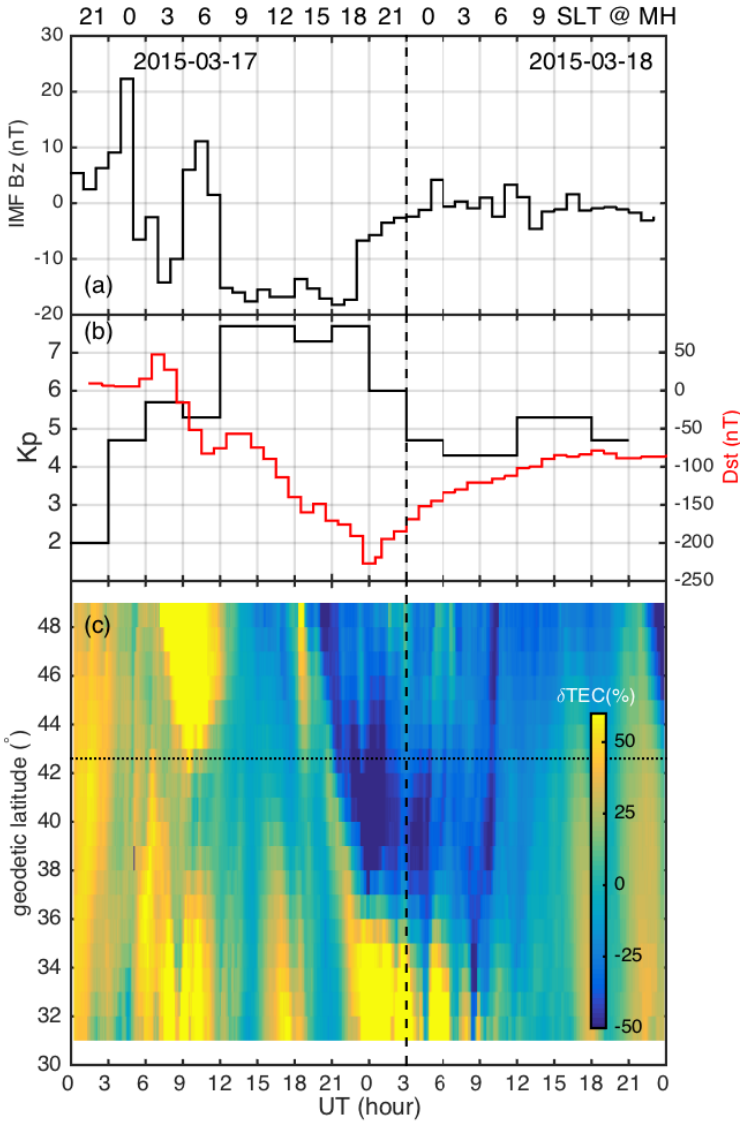

Figure 1. Solar geophysical conditions during March 17-18, 2015: hourly IMF Bz (a), 3-hourly Kp and hourly Dst (b), and GPS TEC disturbances (%) at mid- and subauroral latitudes (c). The TEC is a 3° latitudinal bin average over Millstone Hill longitudes (70-80°W), with non-disturbance background subtracted using the monthly average based North America TEC model [NATEC, Chen et al., 2015]. The dashed line is the approximate time of the poleward wind surge.

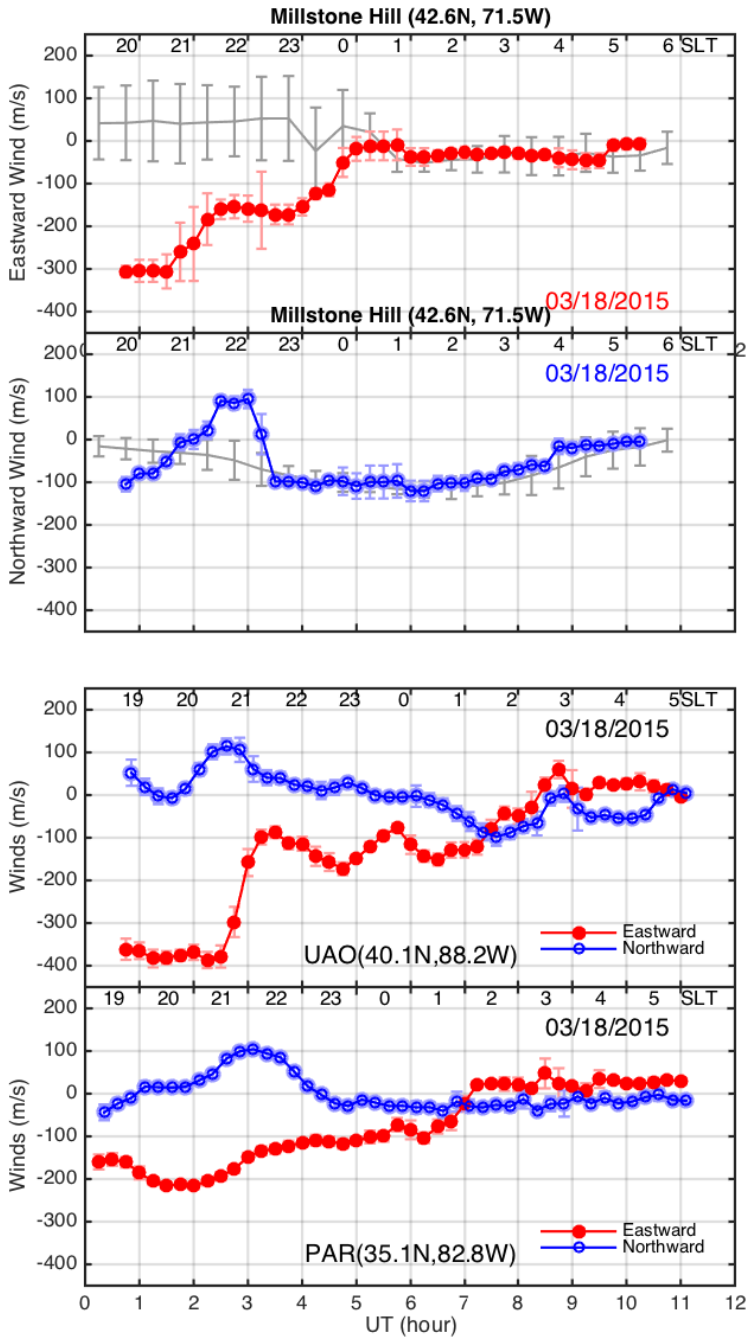

Figure 2. FPI redline neutral winds measured over Millstone Hill (top two panels, gray lines being monthly average and corresponding standard deviation; red and blue curves are winds for 18 March); over UAO and PAR (bottom two panels).

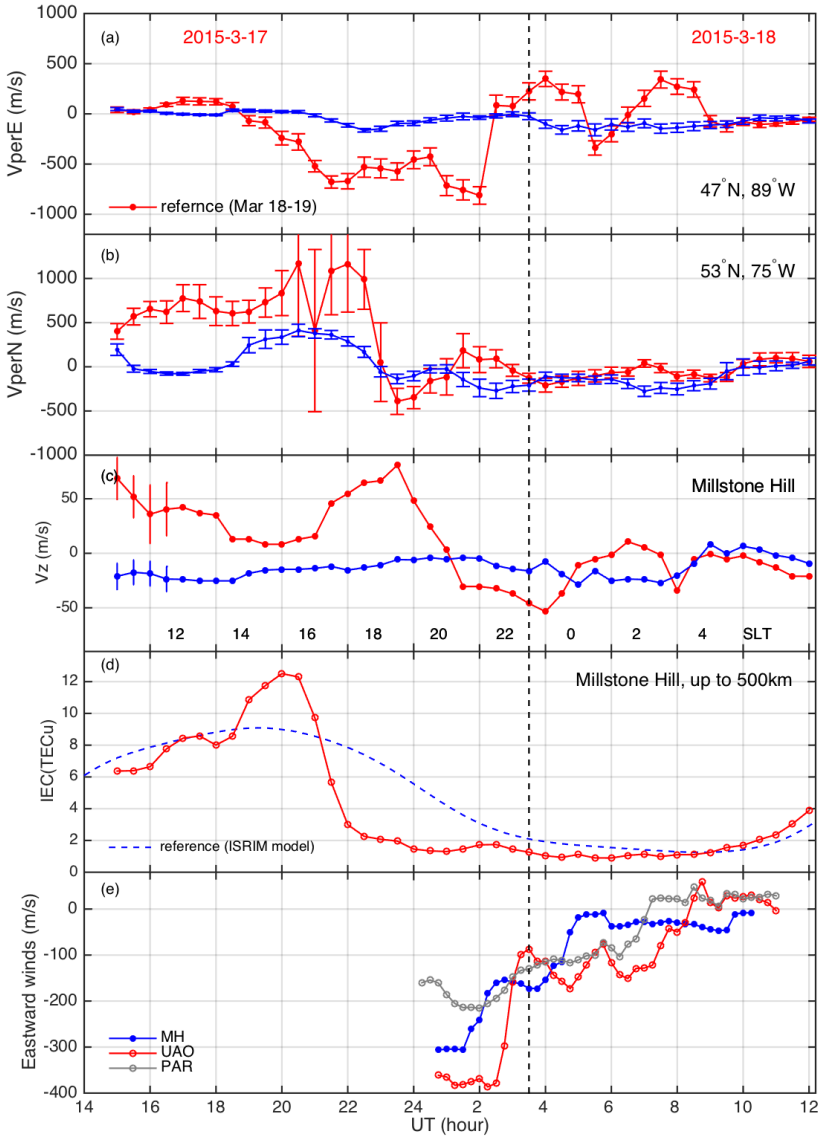

Figure 3. Millstone Hill ISR measurements of plasma drifts VperE (perpendicular east, a) for ~(89°W,47°N), VperN (perpendicular north, b) for ~(75°W, 53°N), vertical upward ion drift Vz at 250 km above MH (c), and integrated ionospheric content IEC (up to 500 km, d). Eastward winds from Figure 2 are also given in (d). The red curves in (a)-(d) are for 17-18 March, and the blue ones in (a) - (c) show reference drift patterns from 18-19 March observations. The dashed blue curve in (d) is a quiet-time reference IEC variation calculated using the ISR empirical ionospheric model ISRIM [Zhang et al., 2007a]. The vertical dashed line indicates the approximate peak time of poleward wind surge.

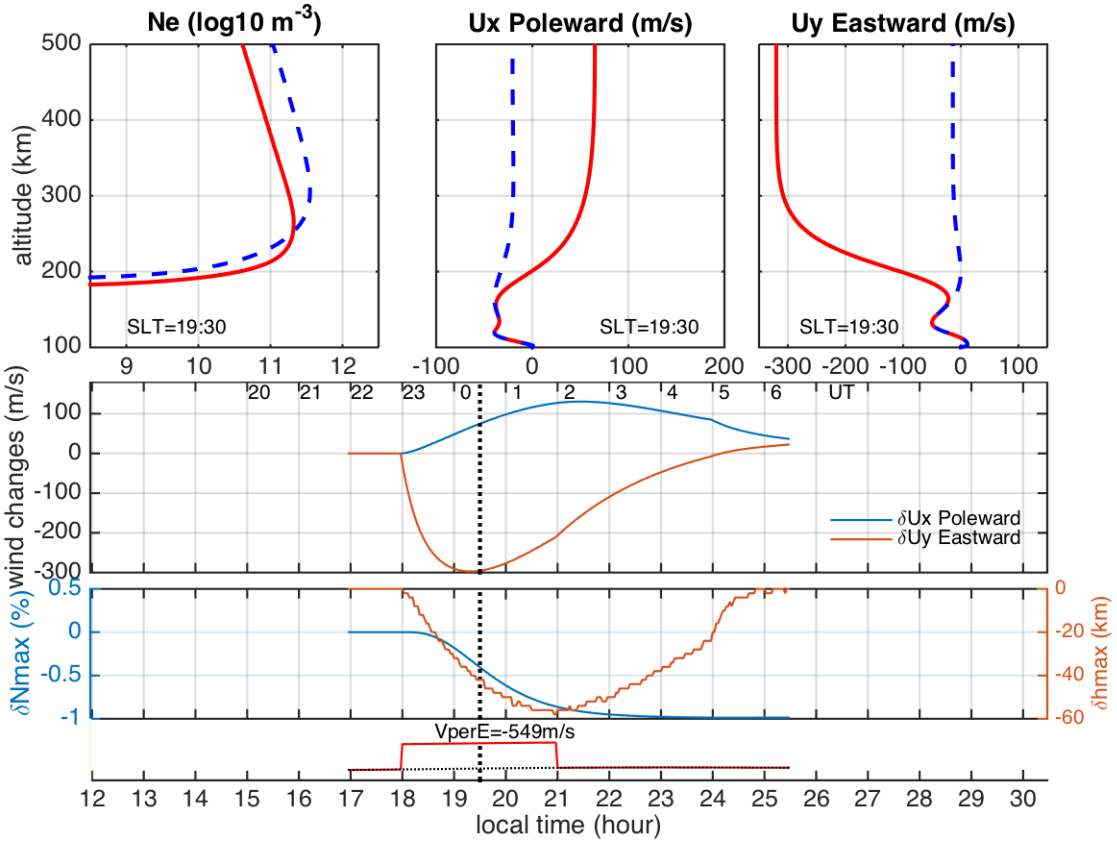

552

553 **Figure 4.** A numerical experiment demonstrates the mechanism of westward ion drift inducing
554 poleward neutral winds over Millstone Hill. A westward ion drift of 500 m/s is applied over 18-
555 20 LT (23-01UT). Profiles on the top panels show results with (red) and without (blue dashed)
556 the strong westward ion drift at 1930 UT for electron density, poleward winds and eastward
557 winds. The middle panel shows corresponding changes in poleward and eastward winds due to
558 inclusion of the strong westward ion drift. The third panel plots simulated changes in the peak
559 electron density (blue) and the peak density height (red). The bottom shows the timing of the
560 injected 500 m/s westward ion drift.